

Structurally Engineered All-Polymeric Microneedle Sensor for Highly Sensitive and Real-Time Monitoring of Glucose in Interstitial Fluids

Ju Hyeon Kim,[†] Chuljin Hwang,[†] and Dae Yu Kim*



Cite This: ACS Sens. 2025, 10, 7025–7034



Read Online

ACCESS |

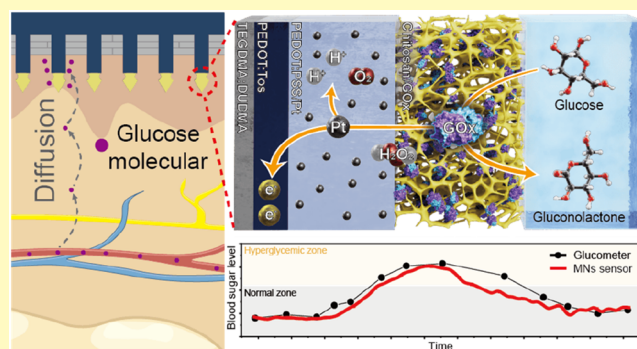
Metrics & More

Article Recommendations

Supporting Information

ABSTRACT: Diabetes mellitus (DM) is a chronic metabolic disorder characterized by persistent hyperglycemia with multiple clinical manifestations and complications, such as cardiovascular disease, kidney dysfunction, retinal impairment, and peripheral neuropathy. Continuous and minimally invasive glucose monitoring is essential for effective DM management. Microneedles (MNs)-based sensing platforms offer a promising solution; however, conventional polymeric MNs suffer from limited electrochemical sensitivity due to their insufficient electroactive surface area and inefficient loading of catalytic and enzymatic components. Herein, we present a fully polymeric, high-sensitive glucose sensor based on structurally engineered mushroom-shaped MNs. The MNs were fabricated from a biocompatible composite of triethylene glycol dimethacrylate (TEGDMA) and diurethane dimethacrylate (DUDMA) and further functionalized with poly(3,4-ethylenedioxythiophene)/tosylate (PEDOT/Tos) to enhance electron transport capabilities. A capillary-driven dip-coating process led to the deposition of Pt nanoparticles (Pt NPs)/PEDOT:PSS composite ink into the neck region of the MNs, resulting in localized loading of electrocatalytic material and a significant increase in electrochemical activity. Consequently, the mushroom-shaped MNs exhibited a 12.6-fold enhancement in current response to glucose compared to conical MNs, while maintaining a linear dynamic range between 2 and 20 mM. Furthermore, *in vivo* validation demonstrated real-time glucose tracking with strong agreement to commercial glucometer readings, and Clarke error grid analysis verified clinical accuracy. Collectively, these results underscore the utility of structural engineering in polymeric MNs to achieve reliable, continuous glucose monitoring for next-generation diabetes care.

KEYWORDS: structural engineering, glucose sensor, microneedle, PEDOT:Tos, sugar template



Diabetes mellitus (DM) is a chronic metabolic disorder characterized by persistent hyperglycemia resulting from insufficient insulin secretion, impaired insulin activity, or a combination of both.^{1–3} Prolonged elevation of blood glucose levels can lead to progressive damage to vital organs, resulting in severe complications, such as cardiovascular disease, kidney dysfunction, retinal impairment, and peripheral neuropathy.^{2,5} The global prevalence of DM is rising rapidly, with 537 million individuals affected in 2021 and projections reaching 783 million by 2045.^{6,7} Given the growing global burden, there is an urgent need for continuous glucose monitoring (CGM), which enables timely diagnosis, personalized intervention, and the prevention of long-term complications.^{8–10}

CGM devices have emerged as essential tools in diabetes management, allowing for real-time tracking of blood glucose fluctuations in response to dietary intake, physical activity, and other physiological factors, without requiring repeated skin punctures that can cause tissue damage or increase infection risk.^{11,12} Among them, clinically validated systems developed by Medtronic, Dexcom, and Abbott have been widely adopted in both clinical and personal healthcare settings. Despite their

proven efficacy, current CGM devices typically employ subcutaneous sensing needles measuring 5–13 mm in length, which are inserted into the hypodermis for continuous glucose detection.^{13–16} These devices often have high manufacturing and operational costs, in addition to frequently causing discomfort during application.^{17,18} Moreover, issues such as acupuncture phobia, allergic reactions, and skin irritation can further compromise patient compliance.^{19–21}

An emerging solution to enhance user compliance and reduce pain is the development of minimally invasive glucose-sensing technologies.²² Among these, microneedles (MNs)-based sensors—typically ~1 mm in length—have gained considerable attention for their ability to access interstitial fluid

Received: June 13, 2025

Revised: August 11, 2025

Accepted: September 4, 2025

Published: September 10, 2025



ACS Publications

(ISF) with minimal discomfort.²³ These MNs penetrate the stratum corneum without reaching deeper pain receptors, enabling reliable glucose detection directly from ISF while significantly reducing the invasiveness associated with conventional blood sampling techniques.^{24,25} To fully harness the clinical potential of MNs-based glucose sensors, material selection is critical, as it governs key factors such as cost, mechanical integrity, biocompatibility, scale fabrication, and geometric tunability.^{26,27} Among various candidates, polymers have attracted considerable attention due to their inherent biocompatibility, customizable mechanical properties, and low fabrication cost.^{28–31} Furthermore, unlike early generation MNs fabricated from metal,^{32,33} silicon,^{34,35} ceramic,^{36,37} or glass,^{38,39} polymeric MNs enable versatile geometric designs while maintaining sufficient mechanical robustness.^{40,41}

However, achieving high sensitivity in fully polymeric MNs-based glucose sensors remains challenging due to the difficulty of precisely controlling the electroactive surface area and uniformly integrating catalytic and enzymatic components onto the MN surface. Furthermore, surface properties must be meticulously optimized to guarantee reliable detection of low-concentration glucose in ISF, even in the presence of other biomolecules, such as ions, urea, carbon dioxide, proteins, and nucleic acids. Therefore, careful design and evaluation of MNs structure are essential to optimize the sensing interface for improved sensitivity and specificity.

In this study, we propose a highly sensitive, fully polymeric MNs glucose sensor fabricated using a composite of triethylene glycol dimethacrylate (TEGDMA) and diurethane dimethacrylate (DUDMA). To enhance electron transport, the surface of the MNs was further functionalized with poly(3,4-ethylenedioxothiophene):tosylate (PEDOT:Tos). The MNs glucose sensor features a mushroom-shaped geometry that leads to capillary-driven localization of functional materials, promoting the entrapment of the catalytic Pt NPs/PEDOT:PSS composite within the active sensing region and significantly enhancing electrochemical performance. Moreover, we assessed the mechanical reliability of mushroom-shaped MNs, demonstrating its capability to penetrate the skin without structural failure or deformation of the tip and neck. The fabricated mushroom-shaped MNs glucose sensor demonstrated exceptional sensitivity (8.4 nA/mM per MN) and strong linearity ($R^2 = 0.9983$) across the physiological glucose concentration range in ISF from 2 to 20 mM. Finally, the biomedical applicability of the mushroom-shaped MNs glucose sensor was validated through in vivo testing, showing strong agreement with a commercial blood glucometer and demonstrating reliable accuracy.

MATERIALS AND METHODS

Materials and Reagents. DUDMA, TEGDMA, Phenylbis (2, 4, 6-Trimethylbenzoyl)phosphine oxide (photoinitiator), 3,4-Ethylenedioxothiophene 97% (EDOT), Trichloro (1H,1H,2H,2H-perfluoroctyl)silane, Iron(III) p-toluene sulfonate, Pyridine, Chitosan, glucose oxidase (Gox) (from *Aspergillus niger* type X-S), glutaraldehyde solution, urea, fructose, sucrose, mannose, lactate, isopropyl alcohol, and trypan blue were purchased from Sigma-Aldrich (St. Louis, MO). Pt nanoparticles were purchased from US Research Nanomaterial Inc. (Huston, TX). PEDOT:PSS solution (Clevios PH 1000) was purchased from Heraeus (Hanau, Germany). Poly(dimethylsiloxane) (PDMS) prepolymer (Sylgard 184A) and curing agent (Sylgard 184 B) were purchased from Dow Corning Co., Ltd. (Shanghai, China). Deionized water (resistivity >18 MΩ cm at 25 °C) was utilized throughout the experiment. The 2223H Ag/AgCl

gel electrode was purchased from 3 M (Saint Paul, MN), and isomalt was commercially obtained.

Surface Modification for Detecting Glucose. A PEDOT:Tos coating was applied to form a current collector on the MNs. The precursor solution was prepared by dissolving iron(III) p-toluenesulfonate (15 wt %) and an equimolar amount of pyridine in isopropyl alcohol (IPA), followed by the addition of 40 μL of EDOT per 1 mL of solution. The conductive layer was formed through a dip-coating process in which the MNs were sequentially immersed in the PEDOT:Tos precursor solution. As demonstrated by the ASTM D3359 tape adhesion test (Figure S1), the resulting coating exhibited strong adhesion, with no observable detachment from the lattice-patterned regions.⁴² Pt nanoparticles (Pt NPs)/PEDOT:PSS composite ink, with a concentration of 50 mg/mL, was prepared by vigorously dispersing the components using a vortex mixer for at least 5 min. A PDMS microreservoir with a depth of 150 μm was utilized to achieve precise deposition of the Pt NPs/PEDOT:PSS composite onto the tip surface of the mushroom-shaped MNs. Finally, a biocomposite layer composed of chitosan hydrogel and GOx was applied using a dip-coating technique to complete the multilayer structure. The chitosan-coated mushroom-shaped MNs were subsequently immersed in a 2 wt % glutaraldehyde solution for 30 s to immobilize the GOx, facilitating covalent cross-linking within the chitosan matrix and stabilizing GOx on the surface of the mushroom-shaped MN.

Surface Characterization. The surface morphology of the modified mushroom-shaped MNs was characterized using scanning electron microscopy (SEM, S-4300SE, Hitachi) operated at an accelerating voltage of 15 kV. Energy-dispersive X-ray spectroscopy (EDS) was conducted on the same surface area to examine the elemental composition, yielding both elemental distribution maps and quantitative weight ratios of specific elements on the surface of the mushroom-shaped MNs.

Skin Insertion Test. To prevent unintended contact with the skin during measurement, a hexahedral structure from a tensile strain machine (Mark-10 Corp., Hicksville, NY) was mounted on the head of a motorized strain gauge. The mushroom-shaped MNs were affixed to this structure using epoxy adhesive. A copper wire was connected to the mushroom-shaped MNs with silver paste, establishing a stable conductive pathway to a source meter (Model 2400, Keithley). Additionally, a commercial Ag/AgCl gel electrode was placed on the back of the researcher's hand and linked to the source meter, forming a closed electrical loop when the mushroom-shaped MNs made contact with the skin. The insertion speed was maintained at a constant rate of 100 mm/min throughout the measurement process.

In-Vitro Glucose Measurement. In-vitro electrochemical measurements were conducted using a conventional three-electrode configuration controlled by an electrochemical workstation (Interface 1010E, Gamry Instruments), which featured a potential resolution of 10 μV and a current sensitivity of 10 pA. An Ag/AgCl electrode served as the reference electrode, whereas a silver plate functioned as the counter electrode. Chronoamperometric measurements were conducted in phosphate-buffered saline (PBS) at an applied potential of 0.4 V, with continuous stirring maintained at 100 rpm.

In-Vivo Glucose Measurement. For in vivo evaluation, the mushroom-shaped MNs glucose sensor was inserted into the researcher's forearm and leg. The glucose concentration in ISF was modulated by the oral ingestion of 40 g of glucose. Concurrently, blood glucose levels were measured using a commercial glucometer (Barozen H, i-SENS Inc., South Korea) and compared with the real-time current signals recorded by the mushroom-shaped MNs glucose sensor.

RESULTS AND DISCUSSION

Fabrication Process of the Fully Polymeric Mushroom-Shaped MN. We developed a multistep molding strategy to fabricate mushroom-shaped MNs with exceptional geometric fidelity and sharp tip definition, as shown in Figure 1A. The process started with the fabrication of a high-

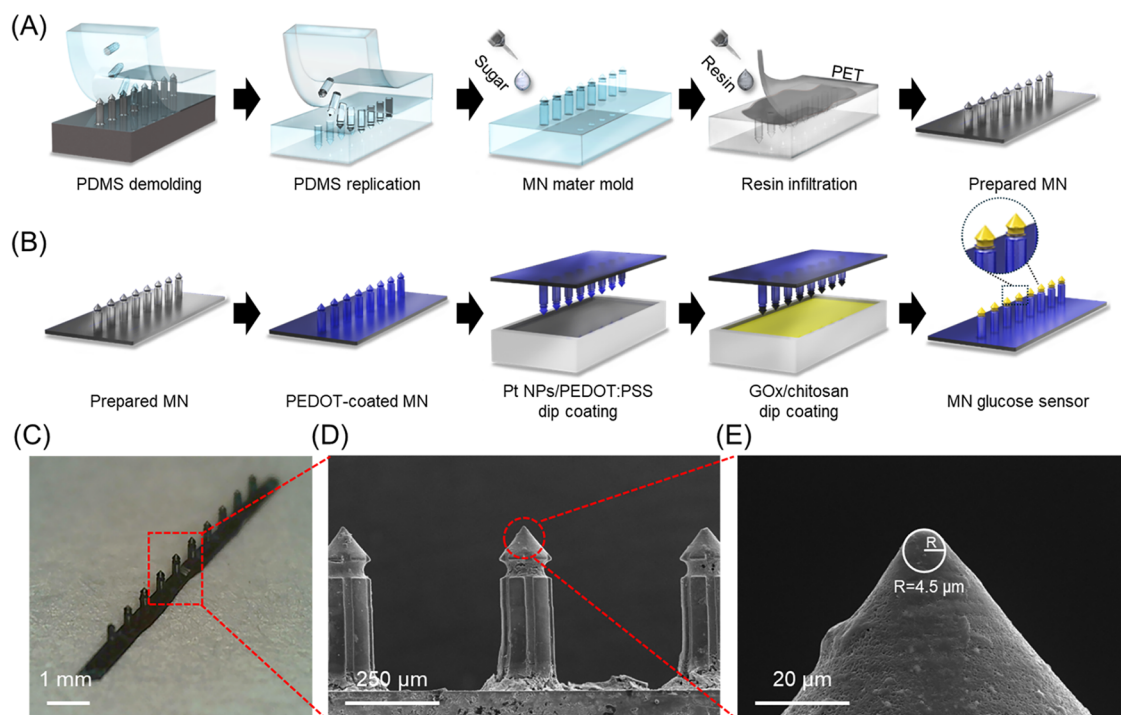


Figure 1. Design and structural characterization of mushroom-shaped MNs. Schematic illustration of the mushroom-shaped MNs glucose sensor, depicting the (A) fabrication process and (B) surface functionalization steps. (C) Bird's eye optical image of the fabricated mushroom-shaped MNs. (D) SEM image of a mushroom-shaped MNs. (E) at a higher magnification, illustrating surface fidelity achieved through the sugar template.

resolution master mold utilizing two-photon polymerization (2PP). Subsequently, a negative mold was produced by casting PDMS over the 2PP master. To mitigate unwanted adhesion during the subsequent molding steps, the surface of the negative PDMS mold was functionalized with a self-assembled monolayer (SAM) using trichloro(1H,1H,2H,2H-perfluoroctyl)silane. A second PDMS casting onto the SAM-treated surface generated a positive mold that accurately replicated the original master features with high fidelity. This positive PDMS mold was then employed to create a sacrificial mold by casting a sugar solution. The sugar mold enabled stress-free demolding by dissolving in water, allowing undamaged separation of the cured polymer without deformation or tip fracture. The sacrificial molding approach demonstrated high reproducibility, with intact demolding and no tip fracture observed over multiple fabrication cycles (Figure S2). In addition, the low oxygen permeability of the sugar mold suppressed oxygen inhibition during subsequent UV curing processes. In the final fabrication step, a monomer composed of TEGDMA and DUDMA was cast onto the sugar mold and polymerized under UV light, resulting in complete cross-linking throughout the MN structure.

Following fabrication as shown in Figure 1B, the mushroom-shaped MNs were sequentially functionalized via dip-coating with PEDOT:Tos, Pt NPs/PEDOT:PSS composite ink, and chitosan hydrogel containing GOx. Each coating step was monitored under an optical microscope to ensure uniform coverage, and the multilayered structures were subsequently dried under refrigerated conditions to stabilize the coatings and preserve enzymatic activity.

Subsequently, the prepared mushroom-shaped MNs were evaluated for geometric uniformity and structural integrity. A bird's-eye optical image demonstrated that the mushroom-shaped MNs were uniformly distributed, exhibiting consistent

geometry across the entire array (Figure 1C). A midmagnification SEM image of four adjacent MNs further validated the regularity of the array and the consistency of their shapes (Figure 1D). Each MN displayed a base diameter of approximately 150 μm , a height of approximately 450 μm , and a center-to-center spacing of 500 μm (Figure S3). A high-magnification SEM image of an individual MN tip (Figure 1E) revealed no structural deformation or surface defects, indicating that the dip-coating process effectively preserved the mold-defined features.

MN Design and Surface Characterization. Current polymer-based MNs structures face significant challenges in achieving the analytical accuracy and reproducibility required for reliable glucose sensing. These limitations are primarily attributed to the challenges of achieving uniform and stable coatings of functional materials on curved, nonplanar polymer substrates.⁴³ In particular, the use of conventional conical geometries often results in uncontrolled reagent distribution during the coating process, thereby introducing signal variability and compromising electrochemical performance. Addressing these challenges requires a precise geometric definition of the reactive interface to enable spatially confined formation of electroactive surfaces.

Figure 2A shows a capillary-driven dip-coating process of the mushroom-shaped MNs. During the withdrawal stage, the meniscus of Pt NPs/PEDOT:PSS composite ink remained pinned at the neck region (Stage 2) and gradually conformed to its equilibrium contact angle along the curved geometry (Stage 3). Upon rupture of the liquid bridge (Stage 4), the Pt NPs/PEDOT:PSS composite ink is predominantly retained in the neck region, with only a minimal residue on the tip, unlike conventional conical MNs (Figure S4). Optical images of the mushroom-shaped MN following the dip-coating and drying process, highlighting the spatial coating of the Pt NPs/

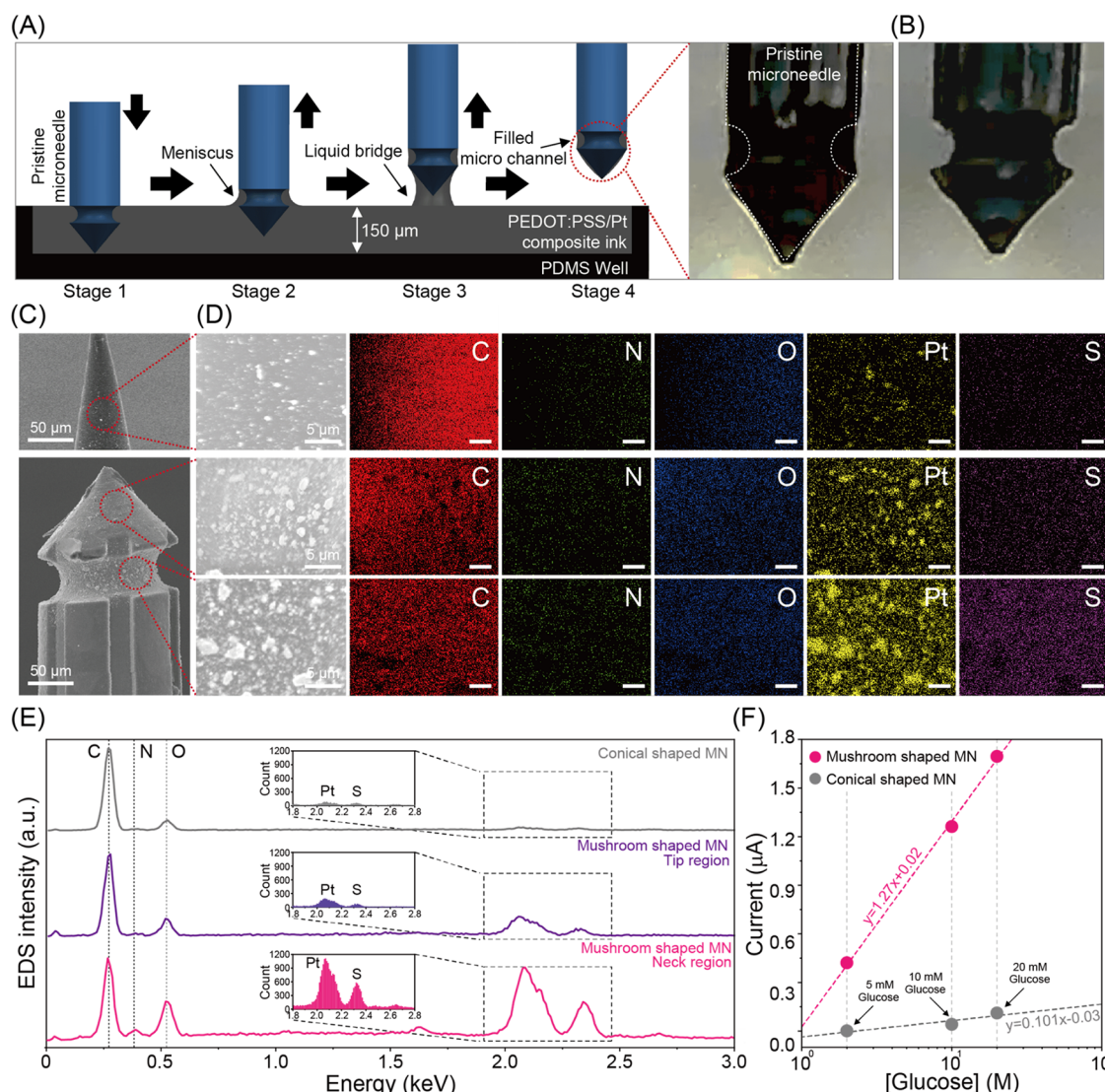


Figure 2. Surface characterization of mushroom-shaped MNs. (A) Schematic of the dip-coating process, which involves sequential formation (the meniscus and the retention of a liquid bridge). (B) Optical image of the mushroom-shaped MNs after drying. (C) SEM images and corresponding (D) EDS elemental maps comparing the surface morphology and elemental distribution of conical and mushroom-shaped MNs after Pt NPs/PEDOT:PSS composite ink coating. The scale bars represent 3 μm . (E) Normalized EDS intensity comparing conical and mushroom-shaped MNs, revealed substantially higher Pt and S signals in the mushroom-shaped geometry. (F) Glucose sensing performance comparison between mushroom-shaped and conical MNs, showing a 12.6-fold increase in current response to glucose for the mushroom-shaped structure.

PEDOT:PSS composite ink, are shown in Figure 2B. Initially retained by capillary action in the neck and tip region, the Pt NPs/PEDOT:PSS composite ink remains localized after solvent evaporation, forming a concentrated coating at the neck region.

Next, we characterized the spatial coating and elemental composition of both conical- and mushroom-shaped MNs using scanning electron microscopy (SEM) and energy-dispersive X-ray spectroscopy (EDS). As shown in Figure 2C, SEM images reveal that conical MNs exhibit sparse and uneven surface coverage, with minimal coating near the tip. In contrast, mushroom-shaped MNs exhibit a dense and uniform coating around the neck region. This morphological distinction is further corroborated by elemental mapping using EDS (Figure 2D), which clearly demonstrates differential spatial distributions of C, N, O, Pt, and S between the two MN structures. The enhanced Pt and S signals indicate localized enrichment of the Pt NPs/PEDOT:PSS composite, likely

driven by capillary effects inherent to the concave geometry. Quantitative EDS analysis (Figure 2E) further verified this observation, with the mushroom-shaped MN exhibiting substantially higher Pt (47.61 wt %) and S (10.07 wt %) at the neck compared to the conical MN (5.92 wt % Pt, 1.70 wt % S), reflecting more efficient retention of both catalytic and conductive components.

The structural advantages of the mushroom-shaped MN are directly reflected in its glucose sensing performance, as shown in Figure 2F. Chronoamperometric measurements performed across glucose concentrations from 5 to 20 mM revealed that mushroom-shaped MNs exhibited current responses approximately 12.6-fold higher than those of conical counterparts. This enhancement is primarily attributed to the concave neck region of the mushroom-shaped MNs, which provides a geometrically confined area that supports capillary-guided accumulation of the Pt NPs/PEDOT:PSS composite and GOx. Although glucose diffusion to the recessed neck region is

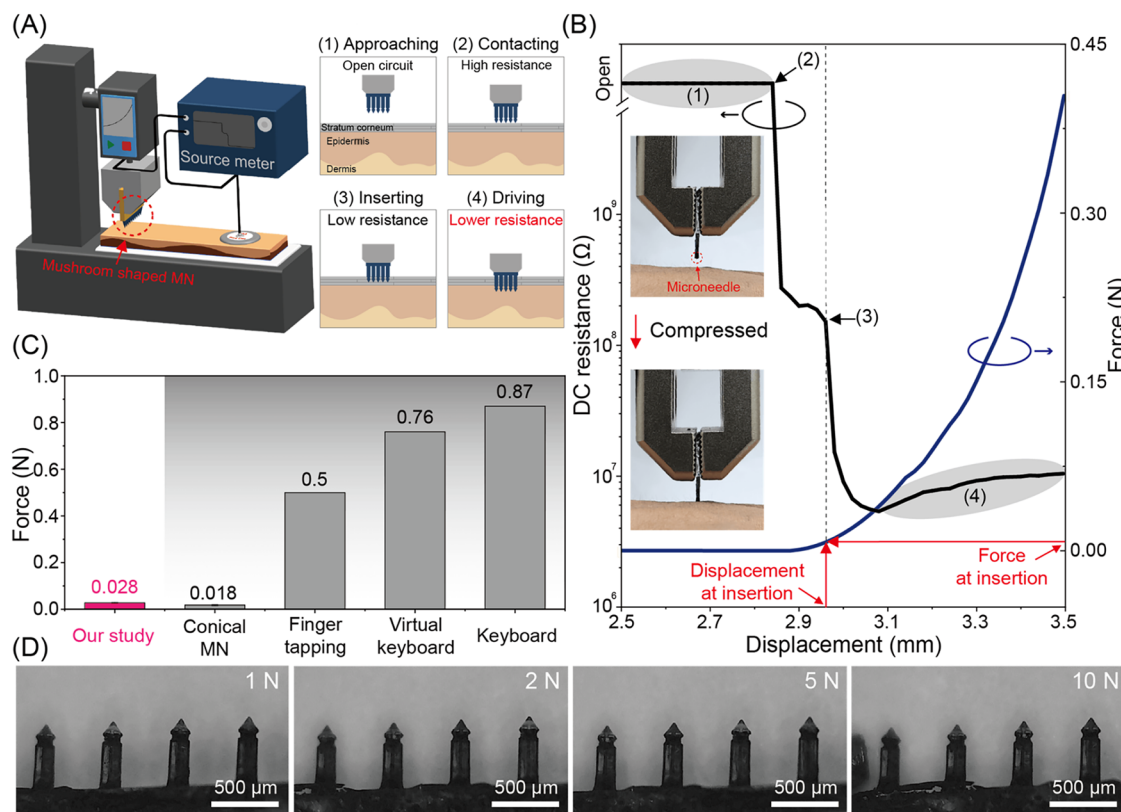


Figure 3. Skin insertion test of mushroom-shaped MNs. (A) Schematic of insertion test setup and the sequential MN-skin interaction stages; (1) approaching, (2) contact, (3) insertion, and (4) driving. (B) Displacement–resistance–force curves (the insets display optical images of the MN before and after insertion) using a source meter and a tensile test machine. (C) Comparative analysis of insertion forces against other common stimuli, highlighting the minimal force required in this study (0.028 N) relative to a conical MN (0.018 N), finger tapping (0.5 N), virtual keyboard (0.76 N), and mechanical keyboard (0.87 N). (D) Optical images of the MNs under increasing applied forces from 1 to 10 N.

slower than to the tip, the increased reactive surface area and elevated GOx loading density effectively offset the reduced mass transport, resulting in robust and enhanced electrochemical responses. These results underscore the critical role of MN architecture in determining electrochemical sensitivity for glucose sensing applications.

Skin Insertion Analysis of Mushroom-Shaped MN. To assess the skin penetration capabilities of the mushroom-shaped MNs, a specialized experimental setup was developed by integrating a tensile testing machine with a source meter (Figure 3A). Notably, insertion tests were conducted on the researcher's forearm, during which displacement, force, and DC resistance were simultaneously recorded to monitor the MN–skin interaction.

As shown in Figure 3B, the insertion process was categorized into four distinct phases based on changes in DC resistance and force. (1) Approaching phase: the mushroom-shaped MNs approached the skin surface without making contact, resulting in an open circuit. (2) Contacting phase: the MNs contacted the stratum corneum, resulting in a sudden drop in resistance within the high-megaohm range and a force increase to approximately 0.003 N, indicating surface compression without penetration. (3) Insertion phase: the MNs penetrated the stratum corneum, as evidenced by a sharp decline in resistance to $151.66\text{ M}\Omega$ and a peak force of 0.028 N, marking the critical threshold for skin penetration. (4) Driving phase: further displacement resulted in deeper insertion and enhanced MN–skin contact. At this stage, resistance stabilized at approximately $5.39\text{ M}\Omega$, whereas the force remained below 0.04 N

owing to soft tissue deformation. Following the electrical and mechanical measurements, trypan blue staining was performed on the researcher's forearm to visually assess skin penetration. The resulting stained insertion sites demonstrated that the mushroom-shaped MNs reliably penetrated the skin (Figure S5).

Figure 3C shows a quantitative comparison of insertion forces associated with the mushroom-shaped MNs, a conical MN, and common mechanical stimuli encountered in daily activities, such as virtual keyboard input and finger tapping.^{44–46} The mushroom-shaped MNs required an insertion force of $0.028 \pm 0.0017\text{ N}$, whereas the conical MN exhibited an insertion force of $0.018 \pm 0.0028\text{ N}$ tested under identical mechanical conditions on the forearm (Figures S6 and S7). Despite the relatively large taper angle of the mushroom-shaped structure, its insertion force remains comparable to that of the conical structure. Notably, the measured insertion force of 0.028 N is substantially lower than the 0.058 N threshold previously reported as necessary for reliable skin penetration, ensuring sufficient mechanical compliance and stable transdermal application without risk of structural failure.⁴⁷ Further comparisons with external mechanical inputs revealed that finger tapping, virtual keyboard usage, and mechanical keyboard pressing required forces of approximately 0.5,⁴⁴ 0.76,⁴⁸ and 0.87⁴⁹ N, respectively. These findings highlight that mushroom-shaped MNs can reliably penetrate the skin with substantially less force than both conical MNs and typical daily mechanical stimuli, demonstrating their ability to achieve reliable insertion with

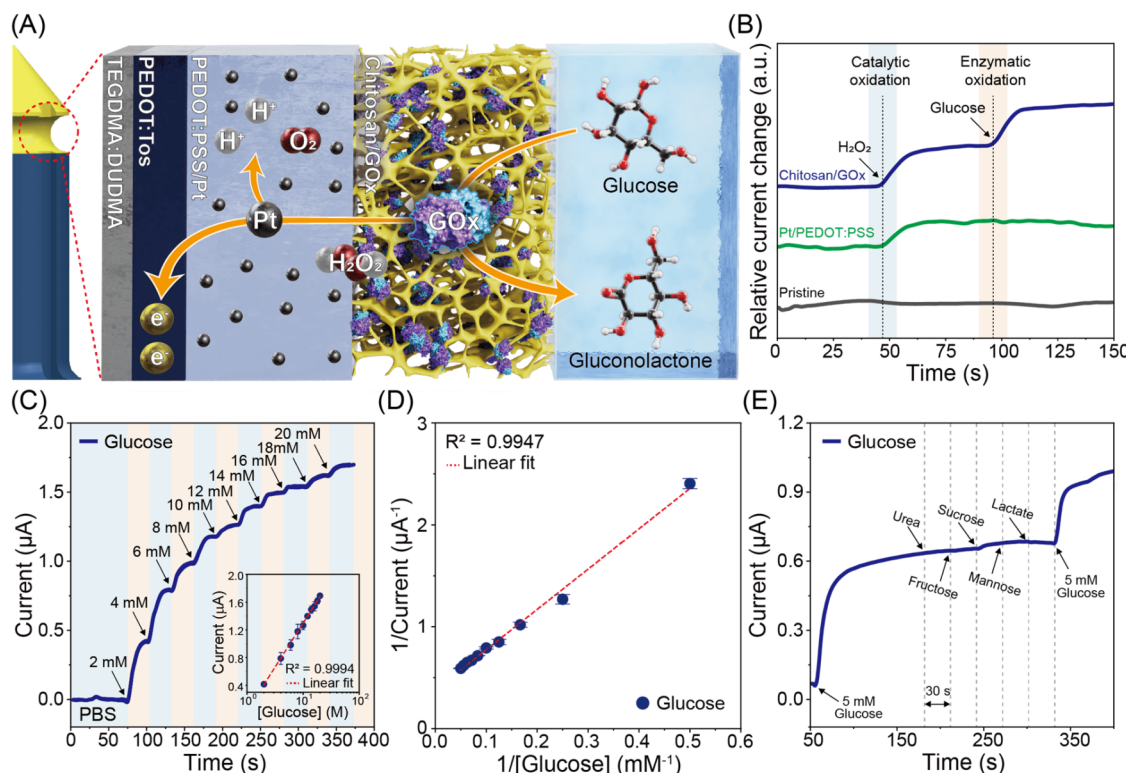


Figure 4. Electrical characteristics of mushroom-shaped MNs glucose sensors in vitro. (A) Schematic of the operational mechanism of the MNs glucose sensor based on catalytic and enzymatic oxidation. (B) Relative current responses of MNs glucose sensors with different surface functionalization upon sequential addition of H_2O_2 and glucose. Only the fully functionalized sensor shows distinct responses to both H_2O_2 and glucose. (C) Real-time current response of the MNs glucose sensor to stepwise additions of glucose (2–20 mM). (D) Lineweaver-Burk plot of the MNs glucose sensor. A linear relationship is observed between the reciprocal of steady-state current and the reciprocal of glucose concentration ($R^2 = 0.9947$). (E) Selectivity characteristics of the MNs glucose sensor, demonstrating current responses to 5 mM glucose compared with potential interfering species, including urea, fructose, sucrose, mannose, and lactate.

minimal force. In addition to mechanical performance, skin compatibility was evaluated after 6 h of sustained skin contact with the MNs glucose sensor. As shown in Figure S8, only faint indentations were observed upon sensor removal, with no visible signs of irritation such as erythema or edema. The skin recovered fully within 1 h, indicating excellent tolerability and minimal disruption to the surrounding tissue during extended use.

Finally, the mechanical robustness of the mushroom-shaped MNs was evaluated under varying compressive loading conditions to assess their structural integrity during insertion (Figure 3D). Vertical forces ranging from 1 to 10 N were applied, and deformation was monitored using side-view optical imaging. Across all tested loads, the MNs maintained their structural integrity, exhibiting no visible bending, fracture, or base deformation. Notably, even under a 10 N compressive load—over 350 times greater than the minimum insertion force of 0.028 N—the tip and body remained intact. These results verified that the mushroom-shaped MNs possess sufficient mechanical strength to enable reliable and effective skin penetration.

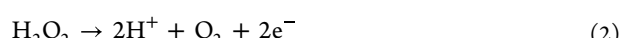
In-Vitro Electrochemical Performance for Detecting Glucose. The electrochemical performance of the mushroom-shaped MNs glucose sensor was evaluated under in vitro conditions (Figure 4A), where a multilayered structure was employed to enable enzymatic glucose recognition and efficient electron transfer. The MNs glucose sensor comprised three functional layers: a top enzymatic layer composed of

GOx embedded within a chitosan hydrogel, a middle catalytic layer consisting of Pt NPs/PEDOT:PSS composite to catalyzes hydrogen peroxide oxidation and electron transport, and a bottom conductive layer of PEDOT:Tos serving as the current collector along the MN surface.

Upon exposure to glucose, GOx catalyzes the oxidation of D-glucose to D-glucono-1,5-lactone and H_2O_2 in the presence of molecular oxygen, as shown in the reaction below



The enzymatically generated H_2O_2 is oxidized at the Pt NPs, and the resulting electrons are transported through the PEDOT:PSS layer and efficiently collected at the PEDOT:Tos conductive interface, resulting in a measurable current, as follows



To assess the electrochemical contribution of each functional layer in the mushroom-shaped MNs glucose sensor, the relative current response following sequential surface modifications was recorded (Figure 4B). Stepwise additions of H_2O_2 and glucose were used as probing analytes. Initially, the PEDOT:Tos-coated MNs exhibited negligible current changes in response to either H_2O_2 and glucose, indicating the absence of catalytic or enzymatic activity without Pt or GOx. Upon coating Pt NPs/PEDOT:PSS composite onto the mushroom-shaped MNs, a distinct increase in current was observed upon

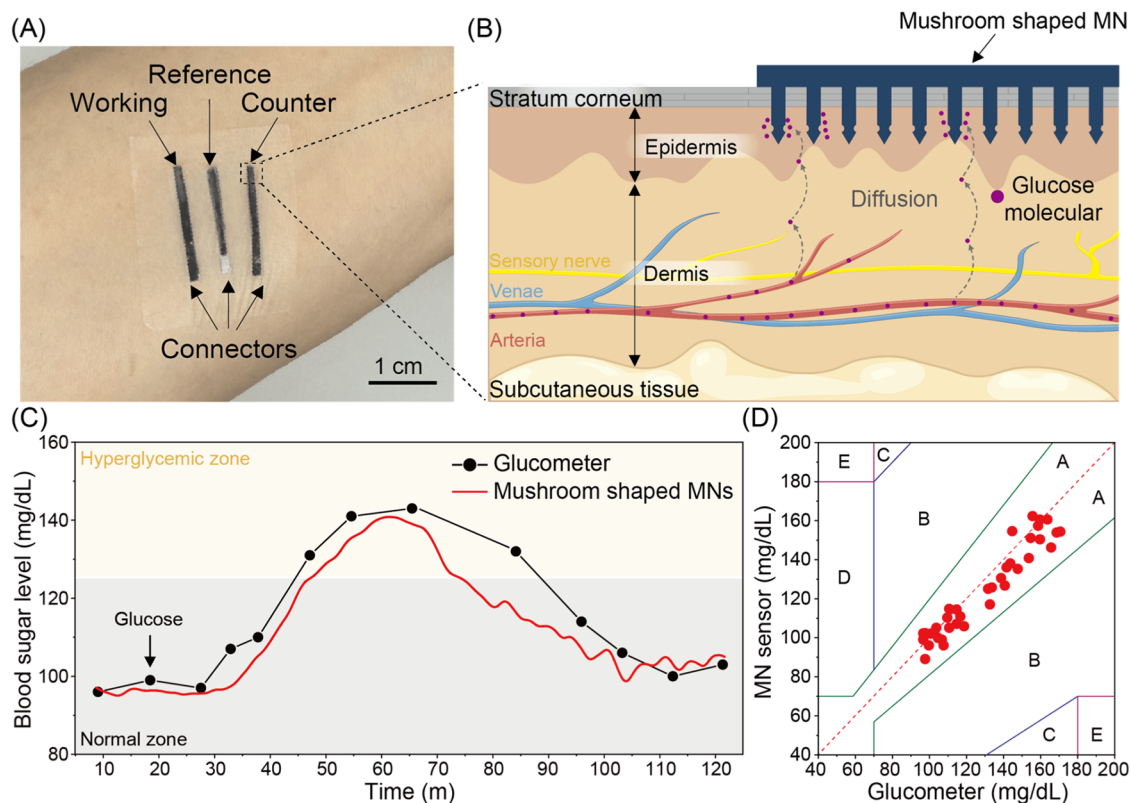


Figure 5. In-vivo evaluation of the mushroom-shaped MNs glucose sensor. (A) Optical image of MNs glucose sensor applied to the skin, highlighting the placement of the working, reference, and counter electrodes. (B) Schematic of the glucose diffusion pathway between the ISF and MNs glucose sensor. (C) Real-time in vivo glucose monitoring utilizing the MNs glucose sensor, compared with a commercial glucometer. The sensor accurately tracked blood glucose fluctuations, with data points consistently aligned within the normal and hyperglycemic ranges over time (black: 13 data points of glucose levels collected using a commercial glucometer; red, glucose concentrations recorded by the MNs glucose sensor). (D) Clarke's error grid analysis showing the detection accuracy of MNs glucose sensor.

H_2O_2 exposure, validating the catalytic functionality of the Pt NPs/PEDOT:PSS composite layer. Subsequent coating of mushroom-shaped MNs using a GOx-embedded chitosan hydrogel led to a pronounced current increase upon glucose addition, clearly indicating the enzymatic activity of the outermost layer. These results highlight the effective surface functionalization of both catalytic and enzymatic layers.

To evaluate the real-time response to glucose, the fully functionalized MNs were subjected to sequential additions of glucose at concentrations ranging from 2 to 20 mM in PBS (Figures 4C and S9). The recorded current exhibited a concentration-dependent increase, reflecting a reliable electrochemical response to physiologically relevant glucose levels. To quantitatively evaluate this behavior, a calibration curve was plotted on a semilog scale (inset of Figure 4C), which revealed exceptional sensitivity (8.4 nA/mM per MN) and excellent linearity ($R^2 = 0.9983$). Although the MNs sensor exhibited robust response characteristics across the tested range, a noticeable reduction in current resolution was observed above 10 mM. This trend is attributed to the small number ($n = 10$) and limited enzyme-loading area of MNs. While this nonlinearity does not affect performance within the physiologically relevant range, enhanced sensitivity at higher concentrations would increase detection accuracy under hyperglycemic conditions. To address this limitation, future studies will investigate raising the number of MNs. In parallel, the MN geometry will be systematically optimized to expand the available surface area for enzyme immobilization,

particularly along the shaft, thereby improving catalytic efficiency and sensor performance. Despite these structural limitations, a comparative analysis of previously reported MN-based glucose sensors (Table S1) demonstrates that our mushroom-shaped MN sensor achieves markedly higher sensitivity, highlighting the advantage of its geometry-guided functionalization strategy.

To gain further insight into the enzymatic reaction kinetics underlying this response, the relationship between glucose concentration and reaction rate was analyzed using a Lineweaver–Burk plot (Figure 4D), which provides a double reciprocal linearization of the Michaelis–Menten equation. A strong linear correlation ($R^2 = 0.9947$) was observed when the reciprocal of the steady-state current was plotted against the reciprocal of glucose concentration, indicating that the sensor response is consistent with classical Michaelis–Menten kinetics characteristic of GOx-mediated glucose oxidation. From the linear fit, the maximum enzymatic rate (V_{\max}) and Michaelis constant (K_m) were determined to be $2.35 \pm 0.071 \mu\text{A}$ and $8.35 \pm 0.52 \text{ mM}$, respectively.

Finally, the selectivity of the mushroom-shaped MNs glucose sensor was evaluated by monitoring the current response following the sequential addition of glucose and various potentially interfering species (Figure 4E). Upon the initial addition of 5 mM glucose at approximately 100 s, a sharp increase in current was observed. By contrast, 5 mM urea, fructose, sucrose, mannose, and lactate produced

negligible changes in current, demonstrating high specificity of the mushroom-shaped MNs for glucose sensing.

In-Vivo Evaluation for Detecting Glucose. To evaluate the in vivo electrical performance of the mushroom-shaped MNs glucose sensor, glucose measurements were conducted on the forearm and leg of a healthy subject (36 years, male), with fingertip blood glucose levels measured by a commercial glucometer serving as a reference. As shown in Figure 5A, the MNs sensor was integrated with a three-electrode configuration and applied to the forearm. The detailed electrical connection of the three-electrode configuration is shown in Figure S10.

The working principle of the MNs sensor is illustrated in Figure 5B. In this configuration, glucose molecules present in the ISF passively diffuse toward the mushroom-shaped MNs, driven by the concentration gradient between the ISF and the enzymatic sensing interface. This diffusion enables enzymatic recognition at the MNs surface, thereby facilitating real-time glucose detection and supporting continuous monitoring of subcutaneous glucose levels without the need for blood sampling.⁵⁰

Figure 5C presents real-time in vivo glucose monitoring performance of the mushroom-shaped MNs sensor in comparison with reference values from a commercial glucometer, with the corresponding raw current signals in Figure S11. The MNs sensor generated a continuous signal (red), whereas the glucometer provided 13 data points (black). Both results exhibited similar temporal trends, with glucose levels ranging from approximately 96 to 146 mg/dL (equivalent to 5.3 to 8.1 mM). To further evaluate clinical accuracy, Clarke error grid analysis was performed. As presented in Figures 5D, S12 and S13, all measured points fell within Zone A—indicating that glucose readings from the MN sensor were within $\pm 20\%$ of reference values. Collectively, these findings demonstrate that the mushroom-shaped MNs glucose sensor delivers reliable, real-time monitoring of subcutaneous glucose levels and aligns closely with standard glucometer readings, highlighting its potential for practical and minimally invasive glucose sensing applications.

CONCLUSIONS

In this study, we developed a fully polymeric MNs glucose sensor designed for real-time, continuous monitoring of glucose levels in both in vitro and in vivo environments. High geometric fidelity and efficient electron transport were achieved by leveraging a mushroom-shaped MNs structure fabricated from a TEGDMA–DUDMA monomer and further functionalized with PEDOT:Tos to enhance electron transport capabilities. Capillary-driven localization of the Pt NPs/PEDOT:PSS composite within the neck region of the mushroom-shaped MNs significantly enhanced the electroactive surface area, leading to a highly sensitive sensing interface. Consequently, the mushroom-shaped MNs exhibited markedly higher current responses, approximately 12.6-fold greater than those of conical MNs. This enhancement enabled a robust and linear electrochemical response across physiologically relevant glucose concentrations, achieving a sensitivity of 8.4 nA/mM per MN within the 2–20 mM range. The mushroom-shaped MNs sensor also exhibited reliable skin penetration without structural failure. In-vivo testing further verified the ability of MNs sensors to provide accurate glucose readings comparable to those from commercial blood glucometers. Collectively, we believe the mushroom-shaped

MNs glucose sensor demonstrates strong potential for next-generation diagnostics by addressing the clinical need for conformable, accurate, and real-time glucose monitoring at point-of-care settings.

ASSOCIATED CONTENT

Supporting Information

The Supporting Information is available free of charge at <https://pubs.acs.org/doi/10.1021/acssensors.5c02073>.

Adhesion robustness of the PEDOT:Tos coating on the TEGDMA-DUDMA substrate (Figure S1); optical images of mushroom-shaped MNs (Figure S2); geometric dimensions of the microneedles (MN) (Figure S3); conical MNs coated with Pt NPs/PEDOT:PSS (Figure S4); skin penetration performance of the MNs (Figure S5); optical image of the fabricated conical MNs (Figure S6); plot of insertion force (Figure S7); photographs of the subject skin (Figure S8); chronoamperometric responses of the mushroom-shaped MNs (Figure S9); schematic illustrating the electrical connections of three-electrode (Figure S10); raw chronoamperometric current response (Figure S11); raw chronoamperometric current response (Figure S12); raw chronoamperometric current response (red) recorded from the MNs (Figure S13); performance comparison of glucose sensor based on MNs (Table S1) ([PDF](#))

AUTHOR INFORMATION

Corresponding Author

Dae Yu Kim – Department of Electrical and Computer Engineering, Center for Sensor Systems, and Inha Research Institute for Aerospace Medicine, Inha University, Incheon 22212, Republic of Korea;  orcid.org/0000-0003-4200-5670; Email: dyukim@inha.ac.kr

Authors

Ju Hyeon Kim – Department of Mechanical Engineering, Inha University, Incheon 22212, Republic of Korea;  orcid.org/0000-0001-7703-0468

Chuljin Hwang – Department of Electrical and Computer Engineering and Center for Sensor Systems, Inha University, Incheon 22212, Republic of Korea;  orcid.org/0000-0001-5646-2077

Complete contact information is available at:
<https://pubs.acs.org/10.1021/acssensors.5c02073>

Author Contributions

[†]J.H.K. and C.H. contributed equally to this work. J.H.K.: Performed formal analysis, investigation, and visualization of figures, and wrote the original draft. C.H.: Performed the biological experiments, analyzed the data, and prepared the figures. D.Y.K.: Performed data analysis and interpretation, conducted project administration, and reviewed the manuscript.

Notes

The authors declare no competing financial interest.

ACKNOWLEDGMENTS

This study was supported by a grant from the National Research Foundation of Korea (NRF) (RS-2018-NR031065, RS-2024-00460600 and RS-2025-00559359). This work was

also supported Korea Medical Device Development Fund grant funded by Korea government (the Ministry of Science and ICT, the Ministry of Trade, Industry and Energy, the Ministry of Health & Welfare, the Ministry of Food and Drug Safety (Project number: RS-2023-00242778)). This research was supported by Korea Institute for Advancement of Technology (KIAT) grant funded by the Korea Government (MOTIE) (RS-2022-KI002581, HRD Program for Industrial Innovation).

■ REFERENCES

- (1) American Diabetes Association. Diagnosis and Classification of Diabetes Mellitus. *Diabetes Care* **2009**, *32* (Supplement_1), S62–S67.
- (2) Antar, S. A.; Ashour, N. A.; Sharaky, M.; Khattab, M.; Ashour, N. A.; Zaid, R. T.; Roh, E. J.; Elkamhawy, A.; Al-Karmalawy, A. A. Diabetes Mellitus: Classification, Mediators, and Complications; A Gate to Identify Potential Targets for the Development of New Effective Treatments. *Biomed. Pharmacother.* **2023**, *168*, No. 115734.
- (3) Hwang, C.; Song, Y.; Baek, S.; Choi, J.-G.; Park, S. Dual-Biased Metal Oxide Electrolyte-Gated Thin-Film Transistors for Enhanced Protonation in Complex Biofluids. *Sci. Rep.* **2024**, *14* (1), No. 30772.
- (4) Catrina, S.-B.; Zheng, X. Hypoxia and Hypoxia-Inducible Factors in Diabetes and Its Complications. *Diabetologia* **2021**, *64* (4), 709–716.
- (5) Demir, S.; Nawroth, P. P.; Herzig, S.; Üstünel, B. E. Emerging Targets in Type 2 Diabetes and Diabetic Complications. *Adv. Sci.* **2021**, *8* (18), No. 2100275.
- (6) Breton, M. D.; Kanapka, L. G.; Beck, R. W.; Ekhlaspour, L.; Forlenza, G. P.; Cengiz, E.; Schoelwer, M.; Ruedy, K. J.; Jost, E.; Carria, L.; Emory, E.; Hsu, L. J.; Oliveri, M.; Kollman, C. C.; Dokken, B. B.; Weinzimer, S. A.; DeBoer, M. D.; Buckingham, B. A.; Cherñavsky, D.; Wadwa, R. P. A Randomized Trial of Closed-Loop Control in Children with Type 1 Diabetes. *N. Engl. J. Med.* **2020**, *383* (9), 836–845.
- (7) Sun, H.; Saeedi, P.; Karuranga, S.; Pinkepank, M.; Ogurtsova, K.; Duncan, B. B.; Stein, C.; Basit, A.; Chan, J. C. N.; Mbanya, J. C.; Pavkov, M. E.; Ramachandran, A.; Wild, S. H.; James, S.; Herman, W. H.; Zhang, P.; Bommer, C.; Kuo, S.; Boyko, E. J.; Magliano, D. J. IDF Diabetes Atlas: Global, Regional and Country-Level Diabetes Prevalence Estimates for 2021 and Projections for 2045. *Diabetes Res. Clin. Pract.* **2022**, *183*, No. 109119.
- (8) Rodbard, D. Continuous Glucose Monitoring: A Review of Recent Studies Demonstrating Improved Glycemic Outcomes. *Diabetes Technol. Ther.* **2017**, *19* (Suppl 3), S-25–S-37.
- (9) Ayers, A. T.; Ho, C. N.; Wong, J. C.; Kerr, D.; Mader, J. K.; Klonoff, D. C. The Benefits of Using Continuous Glucose Monitoring to Diagnose Type 1 Diabetes. *J. Diabetes Sci. Technol.* **2024**, No. 19322968241288923.
- (10) Manov, A. E.; Chauhan, S.; Dhillon, G.; Dhaliwal, A.; Antonio, S.; Donepudi, A.; Jalal, Y. N.; Nazha, J.; Banal, M.; House, J. The Effectiveness of Continuous Glucose Monitoring Devices in Managing Uncontrolled Diabetes Mellitus: A Retrospective Study. *Cureus* **2023**, *15* (7), No. e42545, DOI: [10.7759/cureus.42545](https://doi.org/10.7759/cureus.42545).
- (11) Little, J. P.; Francois, M. E. High-Intensity Interval Training for Improving Postprandial Hyperglycemia. *Res. Q. Exercise Sport* **2014**, *85* (4), 451–456.
- (12) Poolsup, N.; Suksomboon, N.; Kyaw, A. M. Systematic Review and Meta-Analysis of the Effectiveness of Continuous Glucose Monitoring (CGM) on Glucose Control in Diabetes. *Diabetol. Metab. Syndr.* **2013**, *5* (1), No. 39.
- (13) Ahmed, I.; Jiang, N.; Shao, X.; Elsherif, M.; Alam, F.; Salih, A.; Butt, H.; K Yetisen, A. Recent Advances in Optical Sensors for Continuous Glucose Monitoring. *Sens. Diagn.* **2022**, *1* (6), 1098–1125.
- (14) Cappon, G.; Vettoretti, M.; Sparacino, G.; Facchinetto, A. Continuous Glucose Monitoring Sensors for Diabetes Management: A Review of Technologies and Applications. *Diabetes Metab. J.* **2019**, *43* (4), No. 383.
- (15) Hafiz, M. S.; D Campbell, M.; M Orsi, N.; Mappa, G.; Orfila, C.; Boesch, C. Impact of Food Processing on Postprandial Glycaemic and Appetite Responses in Healthy Adults: A Randomized, Controlled Trial. *Food Funct.* **2022**, *13* (3), 1280–1290.
- (16) Cai, Y.; Liang, B.; Chen, S.; Zhu, Q.; Tu, T.; Wu, K.; Cao, Q.; Fang, L.; Liang, X.; Ye, X. One-Step Modification of Nano-Polyaniline/Glucose Oxidase on Double-Side Printed Flexible Electrode for Continuous Glucose Monitoring: Characterization, Cytotoxicity Evaluation and in Vivo Experiment. *Biosens. Bioelectron.* **2020**, *165*, No. 112408.
- (17) Tehrani, F.; Teymourian, H.; Wuerstle, B.; Kavner, J.; Patel, R.; Furmidge, A.; Aghavali, R.; Hosseini-Toudeshki, H.; Brown, C.; Zhang, F.; Mahato, K.; Li, Z.; Barfidokht, A.; Yin, L.; Warren, P.; Huang, N.; Patel, Z.; Mercier, P. P.; Wang, J. An Integrated Wearable Microneedle Array for the Continuous Monitoring of Multiple Biomarkers in Interstitial Fluid. *Nat. Biomed. Eng.* **2022**, *6* (11), 1214–1224.
- (18) Teymourian, H.; Barfidokht, A.; Wang, J. Electrochemical Glucose Sensors in Diabetes Management: An Updated Review (2010–2020). *Chem. Soc. Rev.* **2020**, *49* (21), 7671–7709.
- (19) Gisin, V.; Chan, A.; Welsh, J. B. Manufacturing Process Changes and Reduced Skin Irritations of an Adhesive Patch Used for Continuous Glucose Monitoring Devices. *J. Diabetes Sci. Technol.* **2018**, *12* (3), 725–726.
- (20) Irace, C.; Coluzzi, S.; Di Cianni, G.; Forte, E.; Landi, F.; Rizzo, M. R.; Sesti, G.; Succurro, E.; Consoli, A. Continuous Glucose Monitoring (CGM) in a Non-Icu Hospital Setting: The Patient's Journey. *Nutr. Metab. Cardiovasc. Dis.* **2023**, *33* (11), 2107–2118.
- (21) Rigo, R. S.; Levin, L. E.; Belsito, D. V.; Garzon, M. C.; Gandica, R.; Williams, K. M. Cutaneous Reactions to Continuous Glucose Monitoring and Continuous Subcutaneous Insulin Infusion Devices in Type 1 Diabetes Mellitus. *J. Diabetes Sci. Technol.* **2021**, *15* (4), 786–791.
- (22) Lee, J. E.; Sridharan, B.; Kim, D.; Sung, Y.; Park, J. H.; Lim, H. G. Continuous Glucose Monitoring: Minimally and Non-Invasive Technologies. *Clin. Chim. Acta* **2025**, *575*, No. 120358.
- (23) Takeuchi, K.; Kim, B. Functionalized Microneedles for Continuous Glucose Monitoring. *Nano Convergence* **2018**, *5*, No. 28.
- (24) Saifullah, K. M.; Rad, Z. F. Sampling Dermal Interstitial Fluid Using Microneedles: A Review of Recent Developments in Sampling Methods and Microneedle-Based Biosensors. *Adv. Mater. Interfaces* **2023**, *10* (10), No. 2201763.
- (25) Saifullah, K. M.; Mushtaq, A.; Azarikhah, P.; Prewett, P. D.; Davies, G. J.; Faraji Rad, Z. Micro-Vibration Assisted Dual-Layer Spiral Microneedles to Rapidly Extract Dermal Interstitial Fluid for Minimally Invasive Detection of Glucose. *Microsyst. Nanoeng.* **2025**, *11* (1), No. 3.
- (26) Wang, Y.; Wu, Y.; Lei, Y. Microneedle-Based Glucose Monitoring: A Review from Sampling Methods to Wearable Biosensors. *Biomater. Sci.* **2023**, *11* (17), 5727–5757.
- (27) Lyu, S.; Dong, Z.; Xu, X.; Bei, H.-P.; Yuen, H.-Y.; Cheung, C.-W. J.; Wong, M.-S.; He, Y.; Zhao, X. Going below and beyond the Surface: Microneedle Structure, Materials, Drugs, Fabrication, and Applications for Wound Healing and Tissue Regeneration. *Bioact. Mater.* **2023**, *27*, 303–326.
- (28) Mbituyimana, B.; Ma, G.; Shi, Z.; Yang, G. Polymer-Based Microneedle Composites for Enhanced Non-Transdermal Drug Delivery. *Appl. Mater. Today* **2022**, *29*, No. 101659.
- (29) Meng, F.; Hasan, A.; Babadaei, M. M. N.; Kani, P. H.; Talaei, A. J.; Sharifi, M.; Cai, T.; Falahati, M.; Cai, Y. Polymeric-Based Microneedle Arrays as Potential Platforms in the Development of Drugs Delivery Systems. *J. Adv. Res.* **2020**, *26*, 137–147.
- (30) Kim, H.; Yoon, H.; Sharifuzzaman, M.; Park, J.; Kim, D.; Park, J. Skin-Attachable and Implantable Polymer Microneedle Biosensor for Continuous Glucose Monitoring; 2020 IEEE 33rd International Conference on Micro Electro Mechanical Systems (MEMS); IEEE, 2020; pp 404–407 .
- (31) Piao, H.; Choi, Y.-H.; Kim, J.; Park, D.; Lee, J.; Khang, D.-Y.; Choi, H.-J. Impedance-Based Polymer Microneedle Patch Sensor for

- Continuous Interstitial Fluid Glucose Monitoring. *Biosens. Bioelectron.* **2024**, 247, No. 115932.
- (32) Kolluru, C.; Williams, M.; Chae, J.; Prausnitz, M. R. Recruitment and Collection of Dermal Interstitial Fluid Using a Microneedle Patch. *Adv. Healthcare Mater.* **2019**, 8 (3), No. 1801262.
- (33) Samant, P. P.; Niedzwiecki, M. M.; Raviele, N.; Tran, V.; Menalaix, J.; Walker, D. I.; Felner, E. I.; Jones, D. P.; Miller, G. W.; Prausnitz, M. R. Sampling Interstitial Fluid from Human Skin Using a Microneedle Patch. *Sci. Transl. Med.* **2020**, 12 (571), No. eaaw0285.
- (34) McGrath, M. G.; Vrdoljak, A.; O'Mahony, C.; Oliveira, J. C.; Moore, A. C.; Crean, A. M. Determination of Parameters for Successful Spray Coating of Silicon Microneedle Arrays. *Int. J. Pharm.* **2011**, 415 (1), 140–149.
- (35) Chen, B.; Wei, J.; Tay, F. E. H.; Wong, Y. T.; Iliescu, C. Silicon Microneedle Array with Biodegradable Tips for Transdermal Drug Delivery. *Microsyst. Technol.* **2008**, 14 (7), 1015–1019.
- (36) Vallhov, H.; Xia, W.; Engqvist, H.; Scheynius, A. Bioceramic Microneedle Arrays Are Able to Deliver OVA to Dendritic Cells in Human Skin. *J. Mater. Chem. B* **2018**, 6 (42), 6808–6816.
- (37) Boks, M. A.; Unger, W. W. J.; Engels, S.; Ambrosini, M.; van Kooyk, Y.; Luttge, R. Controlled Release of a Model Vaccine by Nanoporous Ceramic Microneedle Arrays. *Int. J. Pharm.* **2015**, 491 (1), 375–383.
- (38) Wang, P. M.; Cornwell, M.; Prausnitz, M. R. Minimally Invasive Extraction of Dermal Interstitial Fluid for Glucose Monitoring Using Microneedles. *Diabetes Technol. Ther.* **2005**, 7 (1), 131–141.
- (39) Martanto, W.; Moore, J. S.; Kashlan, O.; Kamath, R.; Wang, P. M.; O'Neal, J. M.; Prausnitz, M. R. Microinfusion Using Hollow Microneedles. *Pharm. Res.* **2006**, 23 (1), 104–113.
- (40) Jia, B.; Xia, T.; Wang, X.; Xu, Y.; Guo, Z. Morphology Design of Polymer Microneedle Arrays: Key Factors from the Application Perspective. *J. Drug Delivery Sci. Technol.* **2023**, 88, No. 104883.
- (41) Dabholkar, N.; Gorantla, S.; Waghule, T.; Rapalli, V. K.; Kothuru, A.; Goel, S.; Singhvi, G. Biodegradable Microneedles Fabricated with Carbohydrates and Proteins: Revolutionary Approach for Transdermal Drug Delivery. *Int. J. Biol. Macromol.* **2021**, 170, 602–621.
- (42) D01 CommitteeTest Methods for Rating Adhesion by Tape Test. DOI: 10.1520/D3359-17.
- (43) Pereira, R. L.; Vinayakumar, K. B.; Sillankorva, S. Polymeric Microneedles for Health Care Monitoring: An Emerging Trend. *ACS Sens.* **2024**, 9 (5), 2294–2309.
- (44) Asakawa, D. S.; Crocker, G. H.; Schmaltz, A.; Jindrich, D. L. Fingertip Forces and Completion Time for Index Finger and Thumb Touchscreen Gestures. *J. Electromyogr. Kinesiol.* **2017**, 34, 6–13.
- (45) Kim, J. H.; Aulck, L.; Bartha, M. C.; Harper, C. A.; Johnson, P. W. Are there Differences in Force Exposures and Typing Productivity between Touchscreen and Conventional Keyboard? *Proceedings of the Human Factors and Ergonomics Society Annual Meeting* **2012**, 56 (1), 1104–1108.
- (46) Martin, B. J.; Armstrong, T. J.; Foulke, J. A.; Natarajan, S.; Klinenberg, E.; Serina, E.; Rempel, D. Keyboard Reaction Force and Finger Flexor Electromyograms during Computer Keyboard Work. *Hum. Factors* **1996**, 38 (4), 654–664.
- (47) Sullivan, S. P.; Koutsonanos, D. G.; del Pilar Martin, M.; Lee, J. W.; Zarnitsyn, V.; Choi, S.-O.; Murthy, N.; Compans, R. W.; Skountzou, I.; Prausnitz, M. R. Dissolving Polymer Microneedle Patches for Influenza Vaccination. *Nat. Med.* **2010**, 16 (8), 915–920.
- (48) Kim, J. H.; Aulck, L.; Bartha, M. C.; Harper, C. A.; Johnson, P. W. Are There Differences in Force Exposures and Typing Productivity between Touchscreen and Conventional Keyboard? *Proc. Hum. Factors Ergon. Soc. Annu. Meeting* **2012**, 56 (1), 1104–1108.
- (49) Martin, B. J.; Armstrong, T. J.; Foulke, J. A.; Natarajan, S.; Klinenberg, E.; Serina, E.; Rempel, D. Keyboard Reaction Force and Finger Flexor Electromyograms during Computer Keyboard Work. *Hum. Factors: J. Hum. Factors Ergon. Soc.* **1996**, 38 (4), 654–664.
- (50) Ullah, S.; Hamade, F.; Bubniene, U.; Engblom, J.; Ramanavicius, A.; Ramanaviciene, A.; Ruzgas, T. In-Vitro Model for Assessing Glucose Diffusion through Skin. *Biosens. Bioelectron.* **2018**, 110, 175–179.



CAS BIOFINDER DISCOVERY PLATFORM™

ELIMINATE DATA SILOS. FIND WHAT YOU NEED, WHEN YOU NEED IT.

A single platform for relevant, high-quality biological and toxicology research

Streamline your R&D

CAS 
A division of the
American Chemical Society